

## On the transition from efficient to inefficient line-driving in irradiated flows

RANDALL DANNEN <sup>1</sup>, DANIEL PROGA <sup>1</sup> AND TIM WATERS <sup>2</sup>

<sup>1</sup>*Department of Physics & Astronomy  
University of Nevada, Las Vegas  
4505 S. Maryland Pkwy  
Las Vegas, NV, 89154-4002, USA*

<sup>2</sup>*Theoretical Division, Los Alamos National Laboratory*

Submitted to ApJ

### ABSTRACT

Observations of ionized AGN outflows have provided compelling evidence that the radiation field transfers both momentum and energy to the plasma. At parsec scale distances in AGN, energy transfer can dominate, in which case the only force needed to launch an outflow is that from gas pressure. Much closer to the black hole, gravity dominates thermal energy due to insufficient heating by the radiation and the gas is in the so-called ‘cold’ regime. Only magnetic or radiation forces can then lead to outflow, but it is unclear at what temperature and ionization state the radiation force weakens, as these properties depend on the spectral energy distribution (SED). In this work, we survey the parameter space of radiation forces due to spectral lines resulting from blackbody SEDs with varying temperatures in the range  $\sim 10^4 - 10^6$  K to identify the radiation temperature at which line-driving begins to lose efficiency. We find that the temperature  $\lesssim 4 \times 10^5$  K marks the transition to inefficient line driving. We also self-consistently compute the heating and cooling balance to estimate the gas temperature, so that our parameter survey covers the transition where thermal driving goes from negligible to comparable to line driving. We summarize a large set of hydrodynamical simulations of radial flows to illustrate how the wind properties change during the transition and the dependence of these properties on the assumed SED and governing flow parameters.

*Keywords:* galaxies: active - methods: numerical - hydrodynamics - radiation: dynamics

### 1. INTRODUCTION

Radiation can play a significant role in launching and accelerating mass outflows in active galactic nuclei (AGN) and in other astrophysical systems such as OB stars and cataclysmic variables (CVs). On parsec scale distances in AGN, where there is a weak gravitational potential, energy transfer from radiation to the plasma can result in considerable heating, allowing thermal driving to produce an outflow. On scales where radiation heating is insufficient because gravitational potential energy dominates thermal energy, it can be a good approximation to initially neglect the gas pressure force altogether; this was done in the line-driven wind

model of [Castor et al. \(1975\)](#); hereafter [CAK](#)) and in the magneto-centrifugal wind model of [Blandford & Payne \(1982\)](#), two classic examples of analytic ‘cold’ wind solutions.

Determining the relative role of thermal and radiation driving is challenging because it requires accurate treatment of a non-trivial coupling between electromagnetic radiation and matter (i.e., the gas opacity and emissivity) from the underlying spectral energy distribution (SED) of the radiation (for textbook reviews, see, e.g., [Mihalas & Mihalas 1984](#); [Castor 2007](#), and references therein). In some applications, accurate treatment may seem unnecessary because one could justify ignoring the radiation force by referring to the rule of thumb that “radiation can heat (cool), but frequently it finds it difficult to push” [Shu \(1992\)](#). However, as many rules of thumb, it does not apply everywhere and radiation can push gas

when the total opacity of the gas,  $\kappa_{\text{tot}}$ , is dominated by the contribution from photon scattering. OB stars and CVs are examples of objects with strong winds and negligible thermal driving. In the upper atmospheres and winds of these objects,  $\kappa_{\text{tot}}$  is dominated by contributions from spectral line transitions, which mostly scatter photons, hence their winds are driven by the line force,  $F_{\text{rad},l}$  (as in [CAK](#)). It is possible that this line driving mechanism is responsible for producing supersonic outflows in AGNs as suggested by numerous observations (e.g., [Foltz et al. 1987](#); [Srianand et al. 2002](#); [Ganguly et al. 2003](#); [Gupta et al. 2003](#); [North et al. 2006](#); [Bowler et al. 2014](#); [Lu & Lin 2018](#); [Mas-Ribas & Mauland 2019](#)) and some theoretical work (e.g., [Mushotzky et al. 1972](#); [Arav & Li 1994](#); [Murray et al. 1995](#); [Proga et al. 2000](#); [Proga 2007](#)).

In OB stars, the so-called overionization problem (e.g., [Arav & Li 1994](#); [Murray et al. 1995](#); [Krolik 1999](#); [de Kool & Begelman 1995](#); [Proga et al. 2000](#)) is not an issue because these objects emit radiation similar to blackbodies (BBs) with low temperatures. Therefore, ionizing photons are produced in small numbers and with low energies compared to CVs or AGN, which have much broader UV continuum spectra due to the presence of a multi-temperature BB disk. We note that SEDs for CVs have ionizing properties that fall somewhere between those of OB stars and AGN, as they do possess a soft X-ray contribution from a boundary layer (e.g., [Frank et al. 2002](#)).

The overionization problem becomes a major concern when modeling AGN outflows, however. Computing the ionization balance is necessary, as it serves as a crucial observational constraint, while also determining the magnitude of the line force. There are two seemingly contradictory observational results to consider. On the one hand, AGN are characterized by very high fluxes in both the UV and X-rays and on the other hand, they possess strong spectral lines from moderately and highly ionized species. The likely explanation for how the ionization balance remains hospitable to the observed line formation is self-shielding, in which the radiation penetrating outflowing gas is filtered through denser regions of plasma near the base of the wind (e.g., [Murray et al. 1995](#); [Proga et al. 2000](#); [Proga & Kallman 2004](#), but see also [Sim et al. 2010](#); [Higginbottom et al. 2014](#)). Developing self-consistent models, therefore, requires coupling hydrodynamical (‘hydro’ for short) simulations of the gas dynamics with ionization balance calculations.

To identify when exactly overionization becomes a problem for line-driving, it is necessary to survey the parameter space of the line force resulting from BB SEDs spanning a broad range of temperatures spanning

$2 \times 10^4$  K to  $10^6$  K, while also self-consistently computing the heating and cooling balance to estimate the gas temperature. This need makes it impractical to employ the most sophisticated approach for coupling matter and radiation, namely a multi-group treatment of radiation hydrodynamics (RHD), as described by [Jiang \(2022\)](#), see also references therein). In the latter, performing calculations with a large number of energy bins as needed to accurately sample SEDs is still not entirely feasible. Indeed, most RHD simulations rely on a ‘gray’ treatment of radiation, i.e. using only the Planck, energy, and flux averaged continuum opacities.

In recent years, we have developed a complementary approach for accounting for both line driving and various radiative heating and cooling processes, including Compton processes, that does not require solving the equations of multi-group RHD ([Dyda et al. 2017](#), [Dannen et al. 2019](#); [D17](#) and [D19](#), respectively). In any particular hydro run, we assume a fixed SED, for which we can construct a grid of photoionization models covering all possible ionization states and temperatures that could be encountered in that run. We then self-consistently couple these ionization balance calculations with the hydrodynamics by interpolating from the grid of photoionization models to evaluate the source terms resulting from the net cooling function and the radiation force. Our approach is computationally inexpensive, which is important for exploring a wide range of parameter space.

This methodology has already proven useful for providing new insights into the problem of AGN outflows. For example, in [Dannen et al. \(2020; hereafter D20\)](#), we studied radial winds driven by AGN SEDs, finding that when winds originate at large radii, thermal driving dominates over line driving. Our analysis there showed that at the wind base, despite the low degree of ionization and an abundance of spectral lines, the line force is weak. This weakness is caused by large optical depths in lines that suppress the line force. On the other hand, further into the wind, the gas is highly ionized and as a result, there are fewer lines available, decreasing the overall line force. The few lines are a manifestation of the overionization problem. In addition, the few lines mean that line cooling is inefficient and the gas experiences runaway heating to various degrees depending on the Compton temperature (e.g., [D17](#); [Waters et al. 2021](#)). Thus, overionization not only suppresses line driving but also enhances thermal driving.

While overionization is a well-known concern, the issue of excessively high optical depth in lines at the wind base is new. In this paper, we thoroughly study this previously unexplored regime of parameter space. The

objective is to identify regions where the radiation force dominates over thermal driving in determining the mass loss rate or terminal velocity (or both). In §2, we describe our methods to arrive at wind solutions by solving the hydrodynamic equations including heating and cooling and line driving. In §3, we present the results of our numerical calculations. We conclude and discuss our results in §4 and note that our paper also includes two appendices: Appendix A contains a summary of the photoionization results that we utilize in our wind models, while Appendix B contains scaling relationships between parameters that are helpful to determine different physical regimes for line driving.

## 2. METHODS

As mentioned above, we described our framework for modeling irradiated outflows from a variety of objects (e.g., stars, accretion disks around stars as well as black holes) in a series of papers (D17; D19; D20). This framework was built upon several previous studies of gas outflows in CVs and AGN (e.g., Proga et al. 1998, 2000; Proga 2007).

### 2.1. Photoionization calculations

In D17, we demonstrated our method for modeling outflows resulting from the irradiation of optically thin gas by a radiation field with an *arbitrary* strength and SED. We used the photoionization code `XSTAR`<sup>1</sup> (Kallman & Bautista 2001) to calculate the radiative heating and cooling rates ( $\mathcal{H}$  and  $\mathcal{C}$ , respectively) as functions of gas temperature,  $T$ , and gas ionization parameter

$$\xi = (4\pi)^2 \frac{J_X}{n_H}, \quad (1)$$

where  $J_X$  is the integrated mean intensity from 0.1 Ry–1000 Ry and  $n_H$  the hydrogen nucleon number density.<sup>2</sup> We explored several SEDs: those due to unobscured and obscured AGN (hereafter AGN1 and AGN2, Mehdipour et al. 2015), as well as SEDs for hard and soft state X-ray binaries (hereafter XRB1 and XRB2, Trigo et al. 2013, see Fig. 1 in D17), bremsstrahlung, and blackbody (BB). We applied our method to study the hydrodynamics of 1-D spherical winds heated by a uniform radiation field using the magnetohydrodynamic code `ATHENA++` (Stone et al. 2020).

In our followup work, D19, we presented the next step in our development of a self-consistent method to model astrophysical winds. As in D17, we employed

the photoionization code `XSTAR`, this time to compute not only  $\mathcal{H}(\xi, T)$  and  $\mathcal{C}(\xi, T)$  but also the radiation force due to spectral lines using the most complete and up-to-date line list. For a radial flow, the line force  $\mathbf{F}_{\text{rad},l} = M(\xi, t)\mathbf{F}_{\text{rad},e}$ , where  $\mathbf{F}_{\text{rad},e}$  is the radiation force due to electron scattering and  $M$  is the famous force multiplier introduced by CAK. For a given SED, the force multiplier is a function of  $\xi$  and  $T$  and, in addition, of an optical depth parameter,  $t = \sigma_e \rho \lambda_{\text{Sob}}$ , where  $\sigma_e$  is the mass-scattering coefficient for free electrons,  $\rho$  is the mass density and  $\lambda_{\text{Sob}}$  the Sobolev length. This length is a measure of how much the gas has accelerated relative to thermal velocity and equals to  $v_{th}/(dv_l/dl)$ , where  $v_{th}$  is the thermal velocity while  $dv_l/dl$  is the sight-line velocity gradient. However, to reduce the number of parameters, we assumed the temperature dependence can be captured by using the thermal equilibrium value of  $T$  for a given  $\xi$  so that  $M = M(t, \xi, T_{\text{eq}}(\xi)) = M(t, \xi)$  where  $T_{\text{eq}}(\xi)$  satisfies the equilibrium equation:  $\mathcal{L}(\xi, T_{\text{eq}}) \equiv \mathcal{C}(\xi, T_{\text{eq}}) - \mathcal{H}(\xi, T_{\text{eq}}) = 0$ ,  $\mathcal{L}$  is a net cooling function.

In this paper, our main focus is to present our hydrodynamical simulations. However, we also wish to compile the outcomes of our past and present photoionization computations into a single location. Therefore, we showcase a selection of our results from the photoionization calculations for different SEDs in Appendix A and present a portion of these results in Fig. 1.

Stevens & Kallman (1990) presented one of the earliest quantifications of the overionization problem using detailed photoionization calculations with `XSTAR`. Assuming a 10 keV bremsstrahlung SED, Stevens & Kallman (1990) found that the force multiplier is a strong function of the photoionization parameter for high values of the parameter. In particular, for a given  $t$ ,  $M(t, \xi)$  quickly approaches zero for  $\xi > 100$ . This  $\xi$ -dependence is an illustration of the overionization problem in line-driven winds. The results from Stevens & Kallman (1990) have been applied to model outflows in AGN for over two decades (e.g., Proga et al. 2000; Proga & Kallman 2004; Kurosawa & Proga 2009; Nomura et al. 2013; Waters & Proga 2016; Nomura et al. 2020; Quera-Bofarull et al. 2021; Wang et al. 2022). However, the AGN SEDs differ from a bremsstrahlung SED. Therefore, for given  $\xi$  and  $T$ , the gas exposed to an AGN radiation field can have different spectral lines than that exposed to bremsstrahlung radiation.

In D19, we confirmed that overall the line force is still a strong function of  $\xi$  for high values of  $\xi$  when using AGN SEDs. We also found that for a fixed value of  $t$ , the force multiplier is not a monotonic function of  $\xi$  (see the right panel in Fig. 1 and the first two panels

<sup>1</sup> <https://heasarc.nasa.gov/lheasoft/xstar/xstar.html>

<sup>2</sup> When  $J_X$  is due to a point source so that the ionizing flux is  $F_X = 4\pi J_X$ , this ionization parameter is the familiar  $\xi = 4\pi F_X/n_H$ .

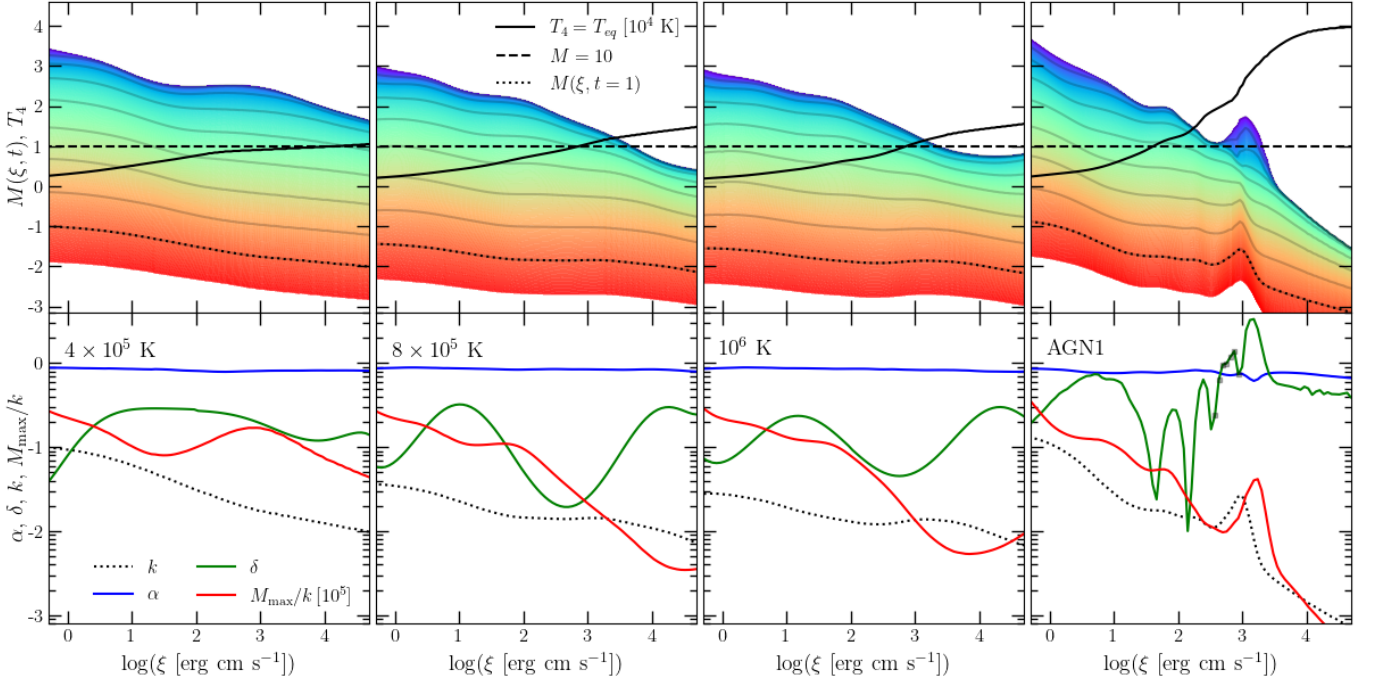


**Figure 1.** Example of results from our photoionization calculations for four SEDs: from left to right, blackbody SEDs with temperatures  $4 \times 10^5$  K,  $8 \times 10^5$  K,  $10^6$  K, and an unobscured AGN SED (AGN1; Mehdipour et al. 2015). *Top panels:* colormaps of the force multiplier for  $t$  decreasing from  $\log t = 1$  (red) to  $\log t = -8$  (blue). Black dotted lines mark  $M(t, \xi)$ , while gray lines indicate  $M(t, \xi)$  at  $\log t = -1, -2, \dots, -8$ , in ascending order, from bottom to top. The horizontal dashed line corresponds to the value  $M(t, \xi) = 10$ , indicating the threshold at which line driving becomes the primary driving force for outflows. The solid black curve (S-curve) corresponds to the equilibrium temperature,  $T_{\text{eq}}$ , in units of  $10^4$  K. *Bottom panels:* profiles of four parameters characterizing the behavior of the force multiplier:  $\alpha(\xi)$ ,  $k(\xi)$ ,  $|\delta(\xi)|$ , and  $M_{\text{max}}(\xi)/k(\xi)$  (blue, black dashed, green, and red curves, respectively). To indicate any negative values of  $\delta$ , we added green squares to the right panel's green line. We calculate the first three parameters along the  $M(t = 1, \xi)$  curves to establish a connection between our numerical findings for the force multiplier and the modified version of the formula proposed by CAK. Finally, we determine the fourth parameter,  $M_{\text{max}}(\xi)/k(\xi)$ , using the  $M(t = 10^{-8}, \xi)$  curve (the highest curve among the curves in the top panels) as a proxy of the maximum force multiplier,  $M_{\text{max}}(\xi)$ . See Appendix A for more details.

in Fig. A.1). While  $M(t, \xi)$  first decreases with  $\xi$  for  $\log \xi \lesssim 2$  as shown by Stevens & Kallman (1990). For both AGN1 and AGN2 SEDs, this decrease is not as strong as compared to a 10 keV bremsstrahlung SED used by Stevens & Kallman (1990). In addition, we found that for a fixed  $t$ ,  $M(t, \xi)$  can increase again at  $\log \xi \approx 1.5$  and more prominently at  $\log \xi \approx 3$  for AGN1. The main consequence of this behavior is that the multiplier remains larger than 1 even at  $\log \xi \approx 3$ , as shown in the right panel in Fig. 1. Moreover, we noted that the range  $10^2 \lesssim \xi \lesssim 10^3$  is also where gas is thermally unstable by the isobaric criterion. The regime of thermal instability (TI; Field 1965) corresponds to the  $\log T$ – $\log \xi$  curve having a slope larger than 1 (see the black solid curve in the top panels in Figs. 1 and A.1).

## 2.2. Hydrodynamical calculations

We solve the equations of hydrodynamics with additional source terms to include radiative and cooling pro-

cesses as well as radiation force:

$$\frac{\partial \rho}{\partial t} + \nabla \cdot (\rho \mathbf{v}) = 0, \quad (2)$$

$$\frac{\partial \rho \mathbf{v}}{\partial t} + \nabla \cdot (\rho \mathbf{v} \mathbf{v} + \mathbf{P}) = -\rho \nabla \Phi + \mathbf{F}_{\text{rad}}, \quad (3)$$

and

$$\frac{\partial E}{\partial t} + \nabla \cdot [(E + p)\mathbf{v}] = -\rho \mathbf{v} \cdot \nabla \Phi - \rho \mathcal{L} + \mathbf{v} \cdot \mathbf{F}_{\text{rad}}, \quad (4)$$

here,  $\rho$ ,  $p$ ,  $\mathbf{v}$ , and  $\mathcal{E}$  are the gas mass density, pressure, velocity, and specific internal energy, respectively. In addition,  $\mathbf{P} = p \mathbf{I}$  where  $\mathbf{I}$  is the unit tensor,  $\Phi = -GM/r$  is the gravitational potential due to a body with mass  $M$ ,  $E = \rho \mathcal{E} + 1/2 \rho |\mathbf{v}|^2$  is the total energy,  $\mathbf{F}_{\text{rad}} = F_{\text{rad}} \hat{\mathbf{r}}$  is the radiation force, and  $\mathcal{L}$  is the net cooling rate. We adopt an adiabatic equation of state  $p = (\gamma - 1)\rho \mathcal{E}$  and assume  $\gamma = 5/3$  in the cases where radiative heating and cooling are present. However, we also consider nearly isothermal cases where we set  $\gamma = 1.0001$



and  $\mathcal{L} = 0$ . Our time-dependent hydrodynamical simulations are performed in spherical coordinates under spherical symmetry (i.e. assuming radial streamlines).

We use pre-calculated tables of  $\mathcal{L} = \mathcal{L}(\xi, T)$ , which is coupled to the hydro using the backward Euler scheme described in D17. As opposed to the linear interpolation method employed by D17,  $\mathcal{L}(\xi, T)$  is evaluated using a cubic interpolation method from the GSL library as described by Waters et al. (2021), who found that this increases the accuracy by factor of about five. In addition, we apply this interpolation scheme when evaluating the force multiplier tables, which are arrived at by following the methods presented in D19. These grids of photoionization calculations are illustrated in Figure 1.

We initialize the density assuming a hydrostatic atmosphere such that  $\rho(r) = \rho_0 \exp(-\text{HEP}_0(r/r_0 - 1))$  with constant temperature set to be  $T_{\text{eq}}(\xi_0)$  (for the definition of  $\text{HEP}_0$ , see Eq. B.6 in Appendix B). The initial velocity for the models that include heating and cooling is set to 0. However, for the isothermal models, we apply the velocity field  $\mathbf{v}(r) = v_{\text{esc}} \sqrt{1 - r_0/r} \hat{\mathbf{r}}$ . At the beginning of our simulations, we apply outflow boundary conditions at the inner and outer radii and allow the hydro to evolve for 10-30% of the total run time. We then pause and restart the simulation with constant gradient boundary conditions applied at the outer radius. We also fix the density in the first active zone to the appropriate value as shown in Table 1. Our standard computational domain is defined to occupy the radial range  $r_0 \leq r \leq 100r_0$ , where  $r_0$  is computed based on our assumed value of  $\xi_0$ . In Table 1, we list the main input parameters of our calculations as well as a short summary of how we compute  $r_0$  and  $\rho_0$ . Finally, we adopt logarithmic grid spacing such that  $dr_{i+1} = 1.0099dr_i$  and use  $N_r = 1020$  grid cells in the radial direction.

For comparison purposes, we present models that include line-driving implemented using the prescription from CAK or modified CAK (mCAK hereafter). These have the force multiplier given by the formula

$$M(t, \xi) = k(\xi)t^{-\alpha}, \quad (5)$$

where  $k(\xi) = k_0 (\xi_0/\xi)^\delta$  (see Appendix A for our explanation of this  $k - \xi$  scaling). In these models, whether or not  $\delta$  is set to zero, we assume  $k_0 = 0.0076$  and  $\alpha = 0.742$ .

### 2.3. Parameter selection

The original application of the CAK theory was to explain mass outflows from OB stars. As we mentioned in §1, the theory has been applied to outflows in CVs and AGNs. In such accretion disk systems, the range

$T_{\text{BB}}$ [K]	$T_0$ [ $10^4$ K]	$\rho_0$ [ $10^{-11}$ g cm $^{-3}$ ]	$r_0$ [ $10^{13}$ cm]	$\Xi_0$
$4 \times 10^5$	5.51	11.1	1.70	28
$8 \times 10^5$	4.76	8.28	1.95	32
$10^6$	4.26	0.66	1.76	26

**Table 1.** Example of input parameters for three SED cases with  $\text{HEP}_0 = 5$ :  $4 \times 10^5$ ,  $8 \times 10^5$ , and  $10^6$  BB SED, the second, third, and fourth columns, respectively. For all models, we assumed  $M = 10 M_\odot$ ,  $\Gamma = 0.2$ , and  $\xi_0 = 80$ . In addition, we set  $T_0$  to  $T_{\text{eq}}$  corresponding to  $\xi_0$  for a given SED. Therefore, the inner radius and the density at the base depend only on  $\text{HEP}_0$  and we compute them using the following expressions  $r_0 = (1 - \Gamma) GM \text{HEP}_0^{-1} c_{s,0}^{-2}$  (see Eq. B.6) and  $\rho_0 = \mu m_p L_{\text{Edd}} \Gamma \xi_0^{-1} r_0^{-2}$ . For reference, we also list  $\Xi_0$  (see Eq. B.11). We explored models with  $\text{HEP}_0$  ranging from 5 to 500 (see Table 2).

of atmospheric temperatures is much wider than among OB stars; in CVs and AGNs, temperatures can be about  $10^3$  K or less and as high as a few  $10^5$  K typically. AGNs have the additional complication that the X-ray source compared to the thermal BB-like source can be significantly stronger than in CVs. To keep our exploration of the various radiative environments general and manageable, we will focus here on BB SED cases with the temperature significantly higher than that applicable to OB stars.

In Table 2, we summarize the main parameters for all simulations that we present in this paper. The table also lists the wind mass loss rate,  $\dot{M}_w$ , momentum efficiency  $\eta_{\text{wind}} \equiv \dot{M}_w v_{\text{out}} c / (L_{\text{Edd}} \Gamma)$  and whether the wind solution reached a steady state or remained variable even after running the simulations for 2 or even 8 sound crossing times (i.e., a few  $100 r_0 / c_{s,0}$ ).

Our illustrative wind simulations are 1D radial flows. Therefore, it may come as a surprise that not all simulations resulted in steady-state solutions akin to time-independent CAK solutions (see right column of Table 2). We have investigated possible causes of this variable behavior and concluded it is not a numerical effect. So as to not limit the results of our parameter survey to steady solutions, these variable solutions have been included in our analysis, with wind properties quoted after time-averaging the solutions. We plan on investigating in more detail the dynamics leading to variability in a future study. In §4, we offer a brief discussion of these variable solutions and cite a couple of previous works that reported on oscillations in the outflows.

## 3. RESULTS

Here, we present our findings on wind solutions for different BB SEDs by focusing on three specific cases: BB SEDs with radiation temperatures  $4 \times 10^5$  K,  $8 \times 10^5$  K, and  $10^6$  K. We selected these cases based on the

Model	HEP	$\dot{M} [M_{\odot} \text{ yr}^{-1}]$	$\eta_{\text{wind}}$	comment
$4 \times 10^5 \text{ K}$	5	$2.99 \times 10^{-7}$	$3.55 \times 10^{-2}$	steady state
	10	$9.78 \times 10^{-8}$	$1.47 \times 10^{-2}$	steady state
	20	$5.21 \times 10^{-8}$	$9.69 \times 10^{-3}$	steady state
	50	$2.67 \times 10^{-8}$	$6.41 \times 10^{-3}$	steady state
	100	$1.71 \times 10^{-8}$	$5.15 \times 10^{-3}$	steady state
	200	$1.12 \times 10^{-8}$	$4.18 \times 10^{-3}$	steady state
	500	$5.28 \times 10^{-9}$	$2.55 \times 10^{-3}$	steady state
$8 \times 10^5 \text{ K}$	5	$2.83 \times 10^{-7}$	$3.82 \times 10^{-2}$	steady state
	10	$1.16 \times 10^{-7}$	$1.69 \times 10^{-2}$	steady state
	20	$2.34 \times 10^{-8}$	$3.13 \times 10^{-3}$	steady state
	50	$2.73 \times 10^{-10}$	$3.05 \times 10^{-5}$	variable
	100	$1.20 \times 10^{-11}$	$5.33 \times 10^{-7}$	variable
	200	$2.46 \times 10^{-13}$	$3.16 \times 10^{-9}$	variable
	500	$1.01 \times 10^{-11}$	$2.18 \times 10^{-6}$	variable
$10^6 \text{ K}$	5	$2.22 \times 10^{-7}$	$3.10 \times 10^{-2}$	steady state
	10	$1.03 \times 10^{-7}$	$1.54 \times 10^{-2}$	steady state
	20	$3.05 \times 10^{-8}$	$4.52 \times 10^{-3}$	steady state
	50	$4.62 \times 10^{-9}$	$9.84 \times 10^{-4}$	steady state
	100	$3.31 \times 10^{-9}$	$1.38 \times 10^{-3}$	variable
	200	$3.20 \times 10^{-9}$	$2.43 \times 10^{-3}$	variable
	500	$2.96 \times 10^{-9}$	$4.54 \times 10^{-3}$	variable
CAK	5	$4.91 \times 10^{-7}$	$5.26 \times 10^{-2}$	steady state
	10	$4.70 \times 10^{-8}$	$6.58 \times 10^{-3}$	steady state
	20	$2.36 \times 10^{-8}$	$6.23 \times 10^{-3}$	steady state
	50	$2.09 \times 10^{-8}$	$9.60 \times 10^{-3}$	steady state
	100	$2.05 \times 10^{-8}$	$1.34 \times 10^{-2}$	steady state
	200	$2.03 \times 10^{-8}$	$1.88 \times 10^{-2}$	steady state
	500	$2.01 \times 10^{-8}$	$2.94 \times 10^{-2}$	steady state
$\delta = 0.1$	5	$4.84 \times 10^{-7}$	$5.13 \times 10^{-2}$	steady state
	10	$3.31 \times 10^{-8}$	$4.09 \times 10^{-3}$	steady state
	20	$9.90 \times 10^{-9}$	$2.21 \times 10^{-3}$	steady state
	50	$7.38 \times 10^{-9}$	$2.75 \times 10^{-3}$	steady state
	100	$6.63 \times 10^{-9}$	$3.44 \times 10^{-3}$	steady state
	200	$6.11 \times 10^{-9}$	$4.38 \times 10^{-3}$	steady state
	500	$5.59 \times 10^{-9}$	$6.13 \times 10^{-3}$	steady state
$\delta = 0.3$	5	$4.73 \times 10^{-7}$	$4.93 \times 10^{-2}$	steady state
	10	$1.91 \times 10^{-8}$	$1.97 \times 10^{-3}$	steady state
	20	$7.33 \times 10^{-10}$	$1.20 \times 10^{-4}$	steady state
	50	$2.60 \times 10^{-10}$	$7.33 \times 10^{-5}$	variable
	100	$1.79 \times 10^{-10}$	$7.07 \times 10^{-5}$	variable
	200	$1.20 \times 10^{-10}$	$6.59 \times 10^{-5}$	variable
	500	$9.14 \times 10^{-11}$	$7.67 \times 10^{-5}$	variable

**Table 2.** List of the simulations considered in this work and summary of some gross properties of the wind solutions. The first column list the model case, from the top to the bottom: self-consistent model with radiative heating and cooling and line driving based on the results from photoionization calculations for  $4 \times 10^5$ ,  $8 \times 10^5$ , and  $10^6$  BB SEDs, isothermal model using the [CAK](#), and two mCAK expressions for line driving with  $\delta = 0.1$  and  $0.3$ . The second column list  $\text{HEP}_0$  value. The third and fourth columns list the wind mass loss rate and momentum efficiency,  $\dot{M}_w$  and  $\eta_{\text{wind}} \equiv \dot{M}_w v_{\text{out}} / (L_{\text{Edd}} \Gamma)$ , respectively. We plot these two and other wind properties as functions of  $\text{HEP}_0$  in Fig. 3. Finally, the last column provides information on whether the wind solution reached a steady state or remained variable.

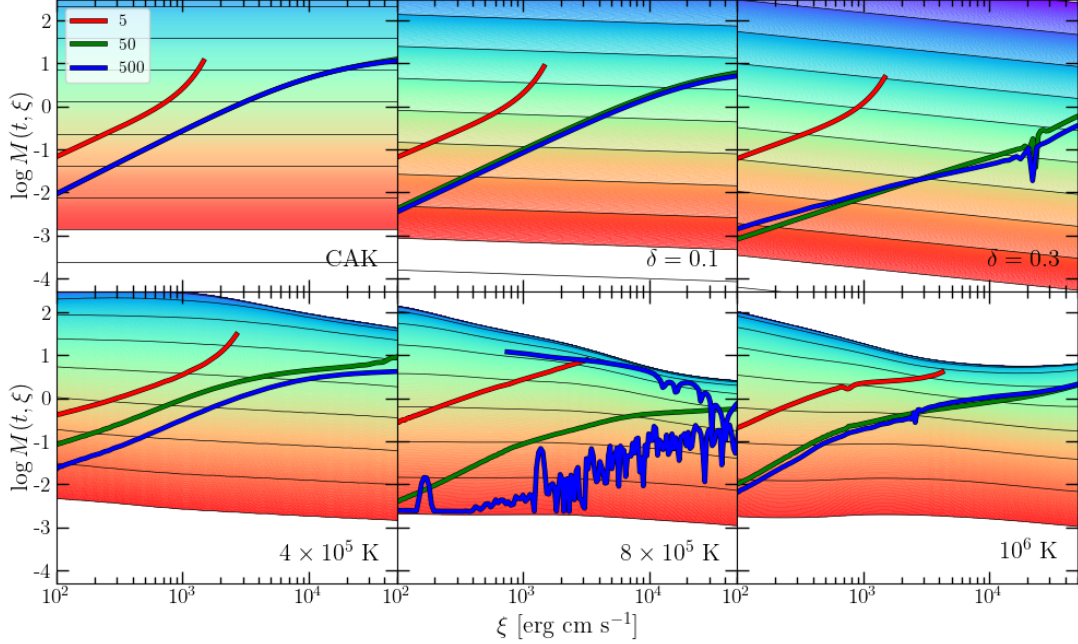


**Figure 2.** The force multiplier as a function of  $\xi$  for a subset of our wind solutions. We present six cases: 1) CAK (i.e.,  $\delta = 0$  top left panel); 2) mCAK with  $\delta = 0.1$  (top middle panel); 3) mCAK with  $\delta = 0.3$  (top right panel); and 4-6)  $4, 8, 10 \times 10^5$  BB SED cases (the bottom panels, from left to right). Each panel shows results of a single snapshot in time for  $\text{HEP}_0 = 5, 50$ , and  $500$  (red, green, blue curves; see Eq. B.6, for the definition of  $\text{HEP}_0$ ). For reference, in each panel, we also plot the force multiplier as a function of  $\xi$  for fixed values of optical depth parameter,  $t$ :  $\log t = -8, -7, \dots, 0, 1$ . In the top panels, the solid lines are by design straight lines, equally spaced and with a slope equal to  $-\delta$  (see the appendix including Eq. A.3). In the bottom panels, the force multiplier is computed based on the photoionization calculations and its  $t$  and  $\xi$  is more complex, for example, the solid lines converge for small  $t$  which reflects the saturation of  $M(t, \xi)$  as  $t$  approaches zero. This saturation is most apparent for the  $8 \times 10^5$  K BB SED case and has a significant effect on the wind solution especially for high  $\text{HEP}_0$  simulations where the solution is highly time dependent. Time dependent behavior manifests on these figures as non-monotonic behavior of  $M$  as a function of  $\xi$  (see Table 2). This is most dramatically shown in the panel corresponding to the  $8 \times 10^5$  K BB SED case, however one can see this effect in the panels for our  $\delta=0.3$  and  $10^6$  K BB SED cases as well.

behavior of the force multiplier (see Figs. 1, A.1, and A.2). The  $4 \times 10^5$  K BB SED case is representative of the regime where the necessary condition for line driving (i.e., inequality B.7 graphically shown as  $M_{max} > 10$ ) is satisfied for a wide range of  $\xi$  whereas the  $8 \times 10^5$  K BB SED and  $10^6$  K BB SED cases are representatives of the regime where the necessary condition is satisfied only for a small or intermediate range of  $\xi$ . We view the  $4 \times 10^5$  K BB SED case as belonging to the class of cases similar to OB stars, where ionization effects are weak or nonexistent. On the other hand, we categorize the latter two cases as belonging to the class of high-temperature BB SED cases, where ionization effects are strong. However, we note that the ionization effects in high-temperature BB SED cases are not as strong as in AGN and XRB cases. Fig. 1 shows the force multiplier and its characteristics for the three selected BB SED cases and for comparison for the AGN1 case. Figs. A.1 and A.2 enable the comparison of the force multiplier in all 14 of our SED cases.

As we mentioned in §2, AGNs emit a significant amount of radiation in the form of ionizing photons that have the potential to completely ionize the gas and cause TI. This is even more true in XRBs. The two figures in Appendix A illustrate this point:  $M_{max}$ ,  $k$ , and  $\eta_{max}$  strongly decrease with increasing  $\xi$  for AGNs and XRBs, which indicates a tendency towards complete ionization of the gas (see corresponding panels in Fig. A.2).

In AGN and XRB cases, the slope of the S curve is greater than 1 for some values of  $\xi$  indicating TI (refer to the solid black curve in the top right panel of Fig. 1 and in the panels corresponding to these SEDs in Fig. A.1). In contrast, all our BB cases are thermally stable, as evident from the slope of the equilibrium curves in  $\log T - \log \xi$  being less than 1 for all  $\xi$  (see again the solid black curves in the top panels in Fig. 1). Thus, we can expect that even for our highest  $T_{BB}$  cases, the wind solution will be qualitatively different from the thermally unstable AGN and XRB cases.

### 3.1. Transition viewed as a function of $\xi$

As we describe in Appendix A,  $M_{max}$  typically decreases with increasing  $\xi$  (see Figs. A.1 and A.2). This downward trend is especially strong for AGN and XRB SEDs and for BB SEDs with  $T_{BB} \gtrsim 4 \times 10^5$  K. However, for  $T_{BB} \lesssim 4 \times 10^5$  K,  $M_{max}$  is relatively high and stays at about the level of 10 even for  $\log \xi$  as high as 5. Thus,  $T_{BB} \approx 4 - 6 \times 10^5$  K marks the transition to the regime for which the line driving will not be significant because the necessary condition for driving is not satisfied for high  $\xi$ .

In Fig. 2, we show how the force multiplier varies as a function of  $\xi$  for 18 different wind solutions. We present results for  $HEP_0 = 5, 50, \text{ and } 500$  (red, green, and blue curves) in six cases: 1) CAK (i.e.,  $\delta = 0$  top left panel); 2) mCAK with  $\delta = 0.1$  (top middle panel); 3) mCAK with  $\delta = 0.3$  (top right panel); and 4-6)  $4 \times 10^5$  K,  $8 \times 10^5$  K and  $10^6$  K BB cases (the bottom panels, from left to right).

The three CAK wind solutions correspond to the case we discuss in Appendix B. For  $HEP_0 \gtrsim 5$ , when the gas is in the cold regime, the wind solution does not depend on  $HEP_0$  as predicted (see also Table 1 and Fig. 3 where we show some gross wind properties as functions of  $HEP_0$ ). For example, in the top left panel of Fig. 2, the curves for  $HEP_0 = 50$  and  $500$  overlap and are different than the red curve corresponding to  $HEP_0 = 5$  which is the hot solution where the wind is driven by the pressure force, not the line force.

In the  $\delta = 0.1$  mCAK case, we also see that the wind solutions for  $HEP_0 = 50$  and  $500$  very similar. Fig. 3 indicates that the transition between the 'hot' to 'cold' solutions (i.e., to those that become insensitive to  $HEP_0$ ) occurs at  $HEP_0 \approx 20$ .

In the other four cases: mCAK with  $\delta = 0.3$ ,  $4 \times 10^5$  K BB,  $8 \times 10^5$  K BB, and  $10^6$  K BB SED, the wind solutions depend on  $HEP_0$  for all  $HEP_0$ . These are the cases where the force multiplier quite strongly decreases with increasing  $\xi$  for a given  $t$  (see, for instance, the slopes of the solid lines plotted in Fig. 2 and the decrease of  $k$  in increasing  $\xi$  in the lower panels of Fig. 1). This decrease in the force multiplier with increasing  $\xi$  results in the weakening of the wind as measured, for example by the wind mass loss rate and velocity in units of the escape velocity that both decrease with increasing  $HEP_0$  for large  $HEP_0$  (see the top and third from the top panel in Fig. 3).

### 3.2. Transition viewed as a function of $HEP_0$

In Appendix A, we cited the expression for  $\dot{M}_{w,CAK}$  (see Eq. B.8) and derived an expression for the line optical depth parameter at the wind base,  $t_0$  (i.e., Eq. B.13). These two quantities are  $HEP_0$  independent for large  $HEP_0$ , under the assumption that  $k$  is a constant. Our numerical solutions for the CAK case are consistent with this prediction as shown by the red lines in Fig. 3. In the other cases that we presented here,  $k$  varies with  $\xi$  either explicitly via a power-law scaling with  $\xi$  or  $v$  (i.e., non zero  $\delta$  in mCAK cases) or implicitly when we use our photoionization calculations. In these cases, the wind solution depends on  $HEP_0$ .

The main physical reason for this  $HEP_0$  dependency can be described in the following way:  $\dot{M}_w$  and other



key wind properties, including  $t_0$  are determined at the wind critical radius ( $r_c$ , see Lamers & Cassinelli 1999, for an overview). To gain insight, one can still refer to eqs. B.8 and B.13 even if the  $k$  parameter decreases as  $\xi$  increases. However, then one must consider the actual value of  $k$  at  $r_c$ .

In our survey, we increase  $\text{HEP}_0$  by decreasing  $r_0$  which results in an increase in the escape velocity,  $v_{esc}$  and a decrease in the flow velocity at the base,  $v_0$  (see Table 1 and the second from left panel in Fig. 4 for specific examples). Thus, as  $\text{HEP}_0$  increases the wind velocity (and also  $\xi$ ) downstream must increase by a large factor in order to reach  $v_{esc}$ , which means that  $k$  at large radii is smaller than at  $r_0$ . Consequently, to maintain the net outward force,  $t$  must decrease and boost the force multiplier by a decrease in the wind density or an increase in the velocity gradient or both.

To explicitly illustrate these dependencies, in Fig. 4, we plot several wind properties and forces acting on the wind as functions of radius for the  $10^6$  K BB SED case and three values of  $\text{HEP}_0$ . The right panel shows explicitly that  $\xi$  at the critical radius increases with increasing  $\text{HEP}_0$  (compare the position of the points marked by the black squares). The right-hand sides of eqs. B.8 and B.13 depend therefore indirectly on  $\text{HEP}_0$  through  $k$ . Formally, there is also indirect dependence through  $\alpha$ . But  $\alpha$  is a very weak function of  $\xi$  even in our self-consistent cases (see the solid blue lines in Figs. 1 and A.1).

Eqs. B.8 and B.13 are of less help to gauge the effects of changes in  $M_{\max}$  or  $\eta$  on the wind properties. But generally one can expect that too large a decrease in  $M_{\max}$  with  $\xi$  will lead to the line force's inability to remain stronger than gravity downstream (see Proga 1999, for an earlier exploration of the effects of the force multiplier saturation on disk and wind solution using a modified CAK method). This limited growth of the force multiplier can prevent the wind from developing, or from being strong like found by Proga (1999) and us here. But moreover the force multiplier saturation can lead to a highly variable wind solution as we found here in high  $\text{HEP}_0$  simulations for the  $8 \times 10^5$  K BB SED cases (see, for instance, the blue line in the bottom middle panel of Fig. 2).

#### 4. DISCUSSION AND CONCLUSIONS

AGNs emit radiation at a significant fraction of their corresponding Eddington luminosities (Giustini & Proga 2019, and references therein). Therefore, the radiation force, including the line force must play a role in at least launching but even accelerating winds from accretion disks in these systems (e.g., Murray et al. 1995; Proga

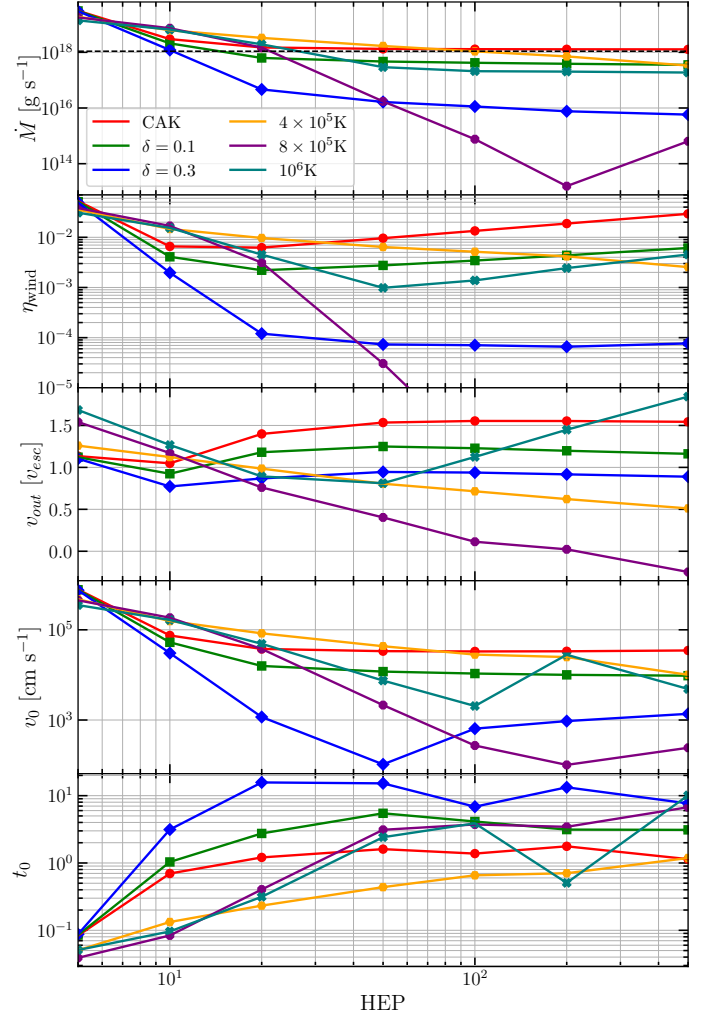


**Figure 3.** Comparison of the gross properties of our wind solutions as a function of  $\text{HEP}_0$ . From top to bottom, those quantities shown are the mass flux, wind momentum efficiency  $\eta_{\text{wind}} = v\dot{M} (c / (\Gamma L_{\text{Edd}}))$ , velocity as the gas exits the outer grid cell in units of escape velocity defined at the inner radius ( $v_{esc} = \sqrt{2GM/r_0}$ ),  $v_{out}$  velocity at the inner radius,  $v_0$ , and optical depth parameter at the inner radius,  $t_0$ . The horizontal black dashed line in the top panel represents  $\dot{M}_{w,\text{CAK}}$  (see Eq. B.8).

et al. 2000; Proga & Kallman 2004; Nomura et al. 2013, 2020). Such radiation-driven disk winds can avoid over-ionization because of self-shielding and can account for the presence of broad absorption lines (BALs; see Giustini & Proga 2019, for a review of both observational and theoretical arguments).

The robustness of the line launching was explored by Proga & Kallman (2004) who considered the "worst case" scenario for line driving of disk winds in AGN. Specifically, they showed that no self-shielding is needed to launch a wind from luminous AGN where  $M_{\text{BH}}$  is very

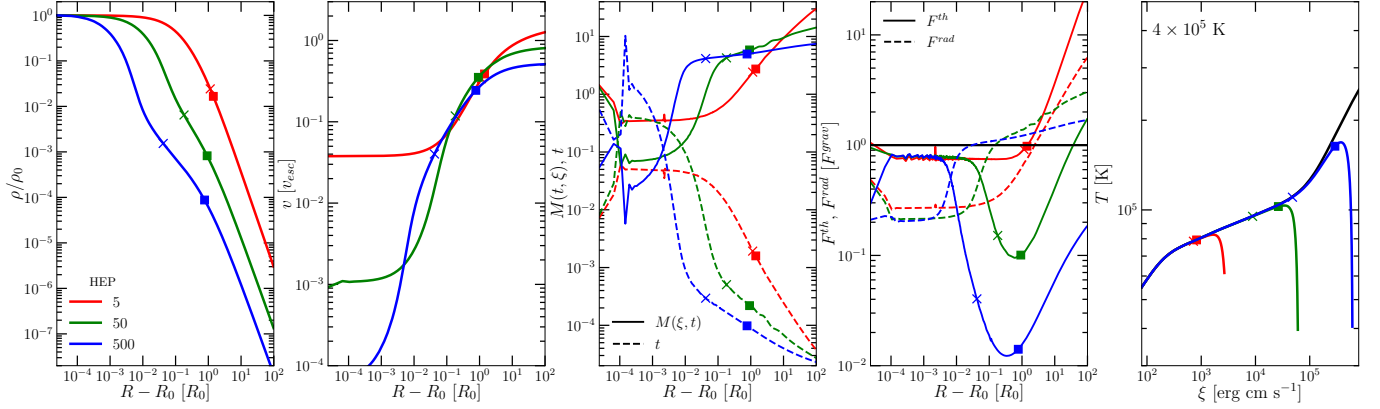


**Figure 4.** Properties of winds for the  $4 \times 10^5$  K BB SED case. We show three solutions that correspond to  $\text{HEP}_0 = 5, 50, 500$  (red, green, and blue lines respectively). Proceeding left to right, the first panel shows the density in units of the density at  $r_0$ ,  $\rho/\rho_0$ . The second panel shows the radial velocity. The third panel shows both the force multiplier,  $M(t, \xi)$  (solid), and the line optical depth parameter,  $t$  (dashed), as functions of radius. The fourth panel displays the radiation force,  $F^{\text{rad}}$ , and gas pressure,  $F^{\text{th}}$ , normalized to the force of gravity,  $F^{\text{grav}}$ , as a function of radius. The final rightmost panel shows the phase diagram (i.e.,  $\log T$  vs.  $\log \xi$ ) for all three wind solutions. The solid black curve corresponds to the thermal equilibrium (“S-curve”, i.e. where  $T = T_{\text{eq}}(\xi)$ ). The x’s and squares in matching colors on each curve mark the sonic and critical radii, respectively).

high (i.e.,  $> 10^8 M_\odot$ ) so that the disk radiation is relatively soft and is dominated by UV radiation. However, they assumed that the force multiplier parameters do not depend on the disk’s local BB SED. This assumption was motivated by the results from modeling of the line driving from OB stars, where it was shown that the energy distribution of the line opacity follows the SED as the star temperature changes and consequently  $k$  and  $\alpha$  do not significantly change with the SED (e.g., Abbott 1982; Lamers & Cassinelli 1999). However, the temperature range in luminous stars is relatively narrow, it ranges from  $10^4$  K to  $5 \times 10^4$  K. This range is certainly narrower than expected in AGN disks where the inner disk temperature can be  $10^5$  K if not enough much more. Thus, it is possible that outside the OB temperature range the line force can significantly depend on the BB SED. In particulate, above some disk temperature,  $k$  can decrease with increasing  $T_{\text{BB}}$ .

It is in this context that we discuss our results here. We surveyed the parameter space of line forces resulting from various temperature BB SEDs, while also self-consistently calculating the heating and cooling rates to compute the temperature. Our main finding is a quantification of how the line force and the wind properties depend on the assumed SED and the key parameters characterizing the wind base such  $\text{HEP}_0$ . Specifically, we found that the line force is relatively insensitive to the BB SEDs with a temperature as high as  $2 \times 10^5$  K, so well above the temperature of OB stars. This means that the line force has a similar capability for launching wind over a wide range of disk radii including the radii

close to the inner disk radius in very high  $M_{\text{BH}}$  where much of the accretion luminosity is liberated.<sup>3</sup>

Our main conclusion is that the line force can operate over a very wide range of SEDs and of the ratio between the gravitational and thermal energies. In other words, this force can operate in both warm and cold regimes, and when the mean photon energy is relatively high, so well beyond the conditions for which the original CAK solutions were obtained, i.e., the cold regime of winds from OB stars. Future modeling of the astrophysical outflows using our method of computing self-consistently the radiative heating and cooling rate and the line force will likely lead to new insights into the properties of line-driven winds, in particular such basic ones like wind efficiency, velocity, and temporal behavior.

#### 4.1. Intrinsically variable wind regime

Here, we found that for some BB SEDs, as  $\text{HEP}_0$  increases, the wind weakens but can reach a steady state. However, there are also some BB SEDs (e.g.,  $8 \times 10^5$  K BB case) in which the wind weakens with increasing  $\text{HEP}_0$  but it does not reach a steady state. These variable winds are in the cold regime, i.e.,  $\text{HEP}_0 \gtrsim 50$ .

The gas in accretion disks in AGN, and also CVs is also in the cold regime. These disks are geometrically thin because their thermal energy is small compared to

<sup>3</sup> This result also indicates that models of mass loss from the central objects of young planetary objects as well as accreting white dwarfs with the surface temperature of the order of  $2 \times 10^5$  K could be viewed as a high-temperature extension of the models for OB stars.

the huge gravitational energy of the central compact object: the corresponding  $\text{HEP}_0$  are large ( $>$  a few thousand even). Proga et al. (1998); Proga (1999) presented results axisymmetric time-dependent simulations of line-driven disk winds. They found a class of wind solutions that are intrinsically variable even though the force multiplier parameters were assumed to be constant, in particular  $k = k_0$ , which corresponds to  $\delta = 0$  (see also Dyda et al. 2020 for a confirmation of this result in the upgraded and 3-D counterparts of these simulations). It is possible then that the process, responsible for wind variability in our simulations, could cause an increased variability in disk winds when  $\delta$  is non-zero, or generally, if the force multiplier parameters are allowed to depend on SED and  $\xi$  as in our models.

In §3, we noted that in the  $8 \times 10^5$  K BB case, the  $\delta$  parameter is relatively high, (i.e.,  $\sim 0.3$ , higher than for typical OB cases, (see, e.g. Lamers & Cassinelli 1999). To elucidate the cause of the variability in our solutions, we have explored a few isothermal cases using a modified CAK method (see Eq. 5). We found that even for these relatively simple cases the wind is variable, even periodic, for  $\delta = 0.3$ . Therefore, we attribute this variability to the weakening of the line force as the wind velocity increases. (recall that  $\delta$  is a measure how quickly  $k$  decreases with increase  $\xi$  or the wind velocity, see Eq. A.3). We plan on further investigating this variable solution. However, two points are worth noting: 1) Curé et al. (2011) studied line-driven winds for various  $\delta$  and stated that they were not able to find any steady-state wind solution in the interval  $0.22 < \delta < 0.30$ . We did find solutions in this interval but they are unsteady; 2) in a stratified atmosphere, the velocity amplitude of the propagating sound waves increases with altitude (e.g., see Clarke & Carswell 2014 for a textbook elaboration on this point). While sound waves form at the base of all line driven winds, only when the line driving is efficiently accelerating the wind (small  $\delta$ ) do these sound waves become stretched at large radii. As opposed to winds where line driving is weak (large  $\delta$ ), this stretching effect is much weaker and therefore, these waves persist even out to large radii. The lower wind velocity which is related to the smaller acceleration appears to be the key: when the acceleration is large the waves are stretched downstream and do not affect the wind,

while when the acceleration is small the wave survey over large distances, and the related pressure force can affect a wind that is driven by a weak line force. Our unsteady wind solutions could also be related to some previously reported radial cases. For example, Owoccki et al. (1994) found that the density at the wind base affects the wind solution including its temporal behavior. Specifically, a steady state transonic outflow exists for a narrow range of  $\rho_0$ . For too small  $\rho_0$ , the outflow is supersonic already at the base whereas for too large  $\rho_0$ . Owoccki et al. (1994) wrote that they "encountered a kind of boundary 'stiffness' that induces a persistent base oscillation in density and velocity." Similar issues were noticed by Proga et al. (1998) and Proga et al. (1999). In addition, Proga et al. (1999) checked how line-driven disk wind solutions depend on the sound speed at the base, which is equivalent to the dependence on  $\text{HEP}_0$ . He found that although the mass loss rate and velocity do not depend on  $c_s$ , the time behavior of the isothermal winds does depend on it. For example, the fiducial state-state solution model from Proga et al. (1998) recalculated with  $c_s$  reduced by a factor of 3 (corresponding to an increase of  $\text{HEP}_0$  by a factor of 3) is somewhat time-dependent: density fluctuations originating in the wind base spread in the form of streams sweeping outward. Generally, he found that wind time dependence weakens with increasing  $c_s$  because the gas pressure effects get stronger with increasing  $c_s$ . Subsequently, higher gas pressure smooths the flow more effectively and in a larger region above the disk mid-plane as the size of the subcritical part of the flow increases with  $c_s$ . Thus, in retrospect, our systematic parameter survey appears to include some cases that have been explored before by others concerned with setting up the lower boundary conditions appropriate to simulate an outflow that is subsonic near the base, goes through a critical point, and becomes supersonic at some finite distance from the base.

## ACKNOWLEDGMENTS

Support for this work was provided by the National Aeronautics and Space Administration under TCAN grant 80NSSC21K0496.

## APPENDIX

### A. DEPENDENCE OF THE FORCE MULTIPLIER ON THE SED AND IONIZATION PARAMETER

Here, we summarize some results from our photoionization calculations of the force multiplier from D17 and D19. Fig. A.1 consists of fourteen pairs of panels for fourteen SEDs (as labeled in each lower panel, with 'temperature

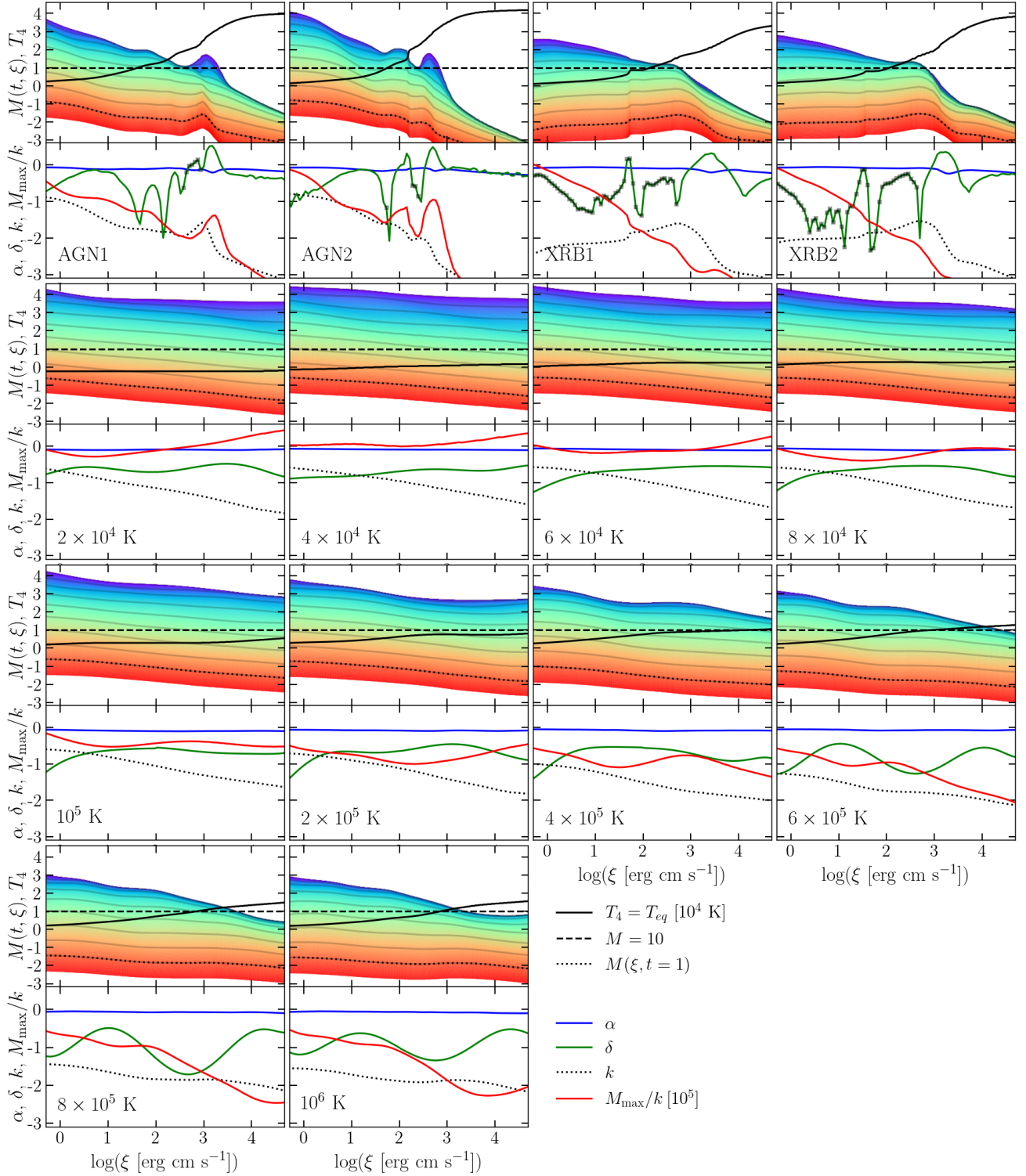


**Figure A.1.** Parameter survey of photoionization results for the two AGNs and two XRBs SEDs (top row of pair of panels), and ten blackbody SEDs of different temperatures. From left to right, from the second top row of panels to bottom, the SEDs correspond to BBs with  $T = 2 \times 10^4$  K,  $4 \times 10^4$  K,  $6 \times 10^4$  K,  $8 \times 10^4$  K,  $10^5$  K,  $2 \times 10^5$  K,  $4 \times 10^5$  K,  $6 \times 10^5$  K,  $8 \times 10^5$  K,  $10^6$  K. The first four SEDs correspond to an unobscured and obscured AGN (AGN1 and AGN2; [Mehdipour et al. 2015](#)) and hard and soft state XRBs (XRB1 and XRB2; [Trigo et al. 2013](#)). *Top panels*: colormap of the force multiplier for  $t$  going from  $\log t = 1$  (red) to  $\log t = -8$  (blue). Black dotted lines mark  $M(t, \xi)$ , while gray lines indicate  $M(t, \xi)$  at  $\log t = -1, -2, \dots, -8$ . The horizontal dashed line marks the value  $M(t, \xi) = 10$ , to indicate the level above which line driving can be the dominant outflow driving mechanism. The solid black line is the equilibrium temperature (or S-curve),  $T_{eq}$ , in units of  $10^4$  K. *Bottom panels*: profiles of  $\alpha(\xi)$ ,  $k(\xi)$ ,  $|\delta(\xi)|$ , and  $M_{max}(\xi)/k(\xi)$  (blue, black dashed, green, and red curves, respectively), the four parameters characterizing the behavior of the force multiplier. To mark negative values of  $\delta$  we added gray squares atop the green line.



labels' indicating the blackbody temperature). In the top panels, we plot the gas equilibrium temperature (solid black curve) as  $T_{\text{eq}}/10^4$  K. The colored bands denote the force multiplier dependence on  $\xi$ ; the thick dotted line is for  $M$  with  $\log t = 0$ , while the other curves are, from the bottom to the top, with  $\log t = -1, -2, \dots, -8$ . The horizontal thick dashed line marks  $M = 10$ . Our results show that regardless of type of the SED, for a fixed  $\xi$ ,  $M(t, \xi)$  asymptotically approaches 0 as  $t$  becomes large and a constant maximum value,  $M_{\text{max}}(\xi)$ , as  $t$  approaches zero; as a proxy for  $M_{\text{max}}(\xi)$ , we use  $M(t = 10^{-8}, \xi)$ . For intermediate values of  $t$ , the force multiplier monotonically increases with decreasing  $t$ .

On the other hand, the dependence on  $\xi$  for a fixed  $t$  can be non-monotonic and specific to a given SED. For example,  $M_{\text{max}}(\xi)$  is of order of a few  $10^3$  for small  $\xi$  in all SED cases, except for the two XRB cases where it is an order of magnitude smaller. As  $\xi$  increases,  $M_{\text{max}}(\xi)$  decreases gradually for the BB SEDs with  $T_{\text{BB}} \lesssim 10^5$  K, strongly for the hotter BB SEDs, and even more strongly for the AGN and XRBs cases. This dependence is not part of the standard parameterization introduced by CAK, so here we analyze it in some detail.

#### A.1. Ionization parameter dependence of the force multiplier I: CAK-like parameterization

It might be possible to capture the force multiplier dependence on both  $t$  and  $\xi$  using some analytic formulae as, for example, [Stevens & Kallman \(1990\)](#) did for a 10 keV bremsstrahlung. However, the fitting parameters would necessarily be specific to a given SED. We opt to instead use the actual results from our photoionization calculations in a tabulated form. Nevertheless, we find that it is instructive and useful to relate our results to some well-known and often-used scaling relations.

The  $t$ -dependence of the force multiplier, including its asymptotic behavior that we found are, unsurprisingly, consistent with the results first found by [CAK](#). They showed that for the large and intermediate values of  $t$ , the force multiplier can be well approximated by the following power law:

$$M_{\text{CAK}}(t) = k_{\text{CAK}} t^{-\alpha}, \quad (\text{A.1})$$

where  $k_{\text{CAK}}$  and  $\alpha$  are constants that can be estimated by fitting the above formula to the results from ionization calculations or using a theoretical approach that considers a statistical distribution of the number of lines as a function of the line opacity and of the line frequency. The saturation of the force multiplier for very small  $t$  corresponds to an optically thin limit for all lines, including the strongest. They estimated that  $M_{\text{max}}$  is of the order of a few  $10^3$  for OB stars.

Motivated by the CAK parameterization, we express  $M(t, \xi)$  as

$$M(t, \xi) = M(t = 1, \xi) t^{-\alpha} \epsilon_{fm} = k(\xi) t^{-\alpha} \epsilon_{fm}, \quad (\text{A.2})$$

where  $M(t = 1, \xi)$  is a normalization factor, which is just a  $\xi$ -dependent version of the  $k_{\text{CAK}}$  parameter (hence the second equality) and  $\epsilon_{fm} = \epsilon_{fm}(t, \xi)$  is a factor correcting the CAK-like scaling for additional dependence of  $M(t, \xi)$  on  $t$  and  $\xi$ . In particular, it accounts for the saturation of  $M(t, \xi)$  as  $t$  approaches zero (see below for more discussion of this point).

To parameterize the force multiplier dependence on ionization at moderate  $t$ , we compute the slope of the force multiplier at  $t = 1$ :  $\delta(\xi) \equiv -\partial \log M(t, \xi) / \partial \log \xi|_{t=1} = d \log k(\xi) / d \log \xi$ . Here, we follow the approach adopted by [Abbott \(1982\)](#) who introduced this parameter to estimate the effect of ionization on the force multiplier through the factor  $(n_{11}/W)^\delta$ , where  $n_{11}$  is the number density in units of  $10^{11} \text{ cm}^3 \text{ s}^{-1}$  and  $W = W(r)$  is the geometrical dilution factor. In our photoionization calculations,  $\delta$  corresponds to that introduced by [Abbott \(1982\)](#) because  $J \propto W$  and using the definition of  $\xi$  (i.e., Eq. 1), one finds that  $\xi \propto W/n$ . We use  $\delta$  to approximate the  $k$ -dependence of  $\xi$ :

$$k(\xi) \simeq k_0 (\xi/\xi_0)^{-\delta}. \quad (\text{A.3})$$

Here,  $k_0$  is the value of  $k(\xi)$  for a fiducial value of the ionization parameter,  $\xi_0$ .

In the bottom panels of Fig. A.1, we plot four parameters characterizing the force multiplier using the convention from [CAK](#) and [Abbott \(1982\)](#). Specifically, we show  $\alpha(\xi) \equiv \partial \log M(t, \xi) / \partial \log t|_{t=1}$  (solid blue curve);  $k(\xi) \equiv M(t = 1, \xi)$  (black dashed curve; note, it is the same quantity shown as the thick black dotted line in the corresponding top panel),  $\delta$  (green curves or green curves with squares if  $\delta$  is negative, i.e., where  $k$  increases with  $\xi$ ) and finally  $M_{\text{max}}(\xi)/k(\xi)$  ( $= M(t = 10^{-8}, \xi)/M(t = 1, \xi)$  in units of  $10^5$ , solid red curve).

The saturation parameter  $\epsilon_{fm}(t, \xi)$  in Eq. (A.2) accounts for an important modification of the original CAK parameterization (i.e., Eq. A.1) which does not have the property  $M(t = 0) = M_{\text{max}}$ . [Owocki et al. \(1988\)](#) first remedied this



by modifying the CAK statistical model through the introduction of a cut off in the maximum line strength, thereby limiting the effect of very strong lines. Specifically, they used the following expression:

$$\epsilon_{fm}(t) = \left[ \frac{(1 + t\eta_{max})^{1-\alpha} - 1}{(t\eta_{max})^{1-\alpha}} \right] = \left[ \frac{(1 + \tau_{max})^{1-\alpha} - 1}{(\tau_{max})^{1-\alpha}} \right], \quad (\text{A.4})$$

where  $\eta_{max}$  is the opacity of the most opaque line and  $\tau_{max} = t\eta_{max}$  ( $\eta_{max}$  is in units of electron scattering opacity). For very large  $\tau_{max}$ , one recovers the original CAK relation since  $\epsilon_{fm} = 1$ , whereas for small  $\tau_{max}$ ,  $\epsilon_{fm} = (1 - \alpha)\tau_{max}^\alpha$  so that the force multiplier becomes  $M_{max} = k_{CAK}(1 - \alpha)\eta_{max}^\alpha$ . Solving this expression for  $\eta_{max}$  gives  $\eta_{max} = [M_{max}/k/(1 - \alpha)]^{1/\alpha}$ , and this expression provides an estimate of the cut-off opacity given the  $\xi$ -dependent parameters  $M_{max}$ ,  $k$ , and  $\alpha$  shown in Fig. A.1:

$$\eta_{max}(\xi) \simeq [M_{max}(\xi)/k(\xi)/(1 - \alpha(\xi))]^{1/\alpha(\xi)}. \quad (\text{A.5})$$

Hence, in general  $\epsilon_{fm}$  can be considered a function of both  $t$  and  $\xi$ .

### A.2. Ionization parameter dependence of the force multiplier II: Analysis

The four parameters  $\alpha(\xi)$ ,  $\delta(\xi)$ ,  $k(\xi)$ , and  $M_{max}(\xi)$  can be used to evaluate the deviation of the force multiplier shown in the top panels of Fig. A.1 from the scaling introduced by CAK. In the CAK scaling,  $\alpha$  and  $k$  are independent of  $\xi$ ,  $M_{max}$  is formally infinite, and  $\delta$  equals 0. For reference, it should be noted that under CAK's scaling, the  $M(t, \xi)$  lines bracketing the colored bands would be purely horizontal and equally spaced from one another (as shown in the top-left panel in Fig. 2).

Our results show that  $\alpha \approx 0.8 - 0.9$  for all BB SEDs, suggesting that it is a relatively very weak function of  $\xi$ . However, for AGN1/2 and XRB1/2 SEDs,  $\alpha$  exhibits a somewhat stronger dependence on  $\xi$  and shows a slight decreasing trend with increasing  $\xi$ . Specifically, it decreases from approximately 0.8 - 0.9 for  $\xi$  values below or equal to  $\log \xi \approx 2$  to around 0.5 - 0.6 for  $\log \xi = 5$ .

The other quantities are more sensitive to  $\xi$  especially for high-temperature BBs and AGN and XRB cases. This was also found by Stevens & Kallman (1990) for the 10 keV bremsstrahlung. The dependence of the force multiplier on  $\xi$  is reflected in a non-zero value of  $\delta$  which could be as high 1 in the cases with relatively hard SEDs. This value of  $\delta$  is much higher than in OB stars where  $\delta < 0.2$  (see for example Table 8.2 in Lamers & Cassinelli 1999, and references therein) and in our results for BBs where  $\delta$  does not exceed 0.4. We note that  $\delta$  is negative for some  $\xi$ , which is an indication that the force multiplier can be a non-monotonic function of  $\xi$  as found by D19. CAK showed  $k$  is related to the total number of spectral lines. Therefore, the dependence of  $k$  on  $\xi$  is related to a variation in total line number, so it is not too surprising that  $\delta$  could be negative for some  $\xi$  (note that a possibility of  $\delta$  being negative in OB star cases has been mentioned by Puls et al. 2000).

The dependence of  $k$  on  $\xi$  is dynamically important because, for example, the wind mass loss rate depends on  $k$  (see Eq. B.8). A visual inspection of our results indicates that the  $k$ - and  $\delta$ - $\xi$  dependencies can be well captured by a single power law for BBs with temperatures  $\lesssim 10^5$  K, while a broken-power-law would be required for higher temperature BBs. The AGN and XRBs cases are more complicated, as both  $k$  and  $\delta$  are non-monotonic functions of  $\xi$ . Piecewise functions (e.g., a combination of several power laws or power laws and exponential functions) would be required, as also found by Stevens & Kallman (1990).

In our hydrodynamical simulations, we have used tabulated values of  $M(t, \xi)$  rather than fits to these values. Nevertheless, the  $\delta$  parameterization of the  $k$ - $\xi$  dependence (see Eq. A.3) has proven to be very useful in interpreting our hydrodynamical results and making a more direct connection with previous work by Abbott (1982) and others.

To facilitate a comparison of the properties of the force multiplier for different SEDs and their trends with  $\xi$ , we show six parameters in Fig. A.2:  $M_{max}$ ,  $k$ , the ratio of  $M_{max}$  and  $k$ , maximum line opacity  $\eta_{amax}$ ,  $\alpha$ , and  $\delta$ . One of the main results shown in this figure is that up to  $T_{BB} \sim 2 \times 10^5$  K, the properties of  $M(t, \xi)$  are not very sensitive to SEDs. For higher temperature SEDs, the force multiplier parameters are sensitive to SEDs and strongly dependent on  $\xi$ , except for the  $\alpha$  parameter which only varies by a factor of 2 across a range of seven orders of magnitude of  $\xi$ , even for the hottest SED.

## B. SCALING RELATIONS

A useful measure of the strength of the thermally driven wind is the ratio of the effective gravitational potential to the thermal energy at the radius of the wind base,  $r_0$ , usually termed the hydrodynamic escape parameter (HEP),

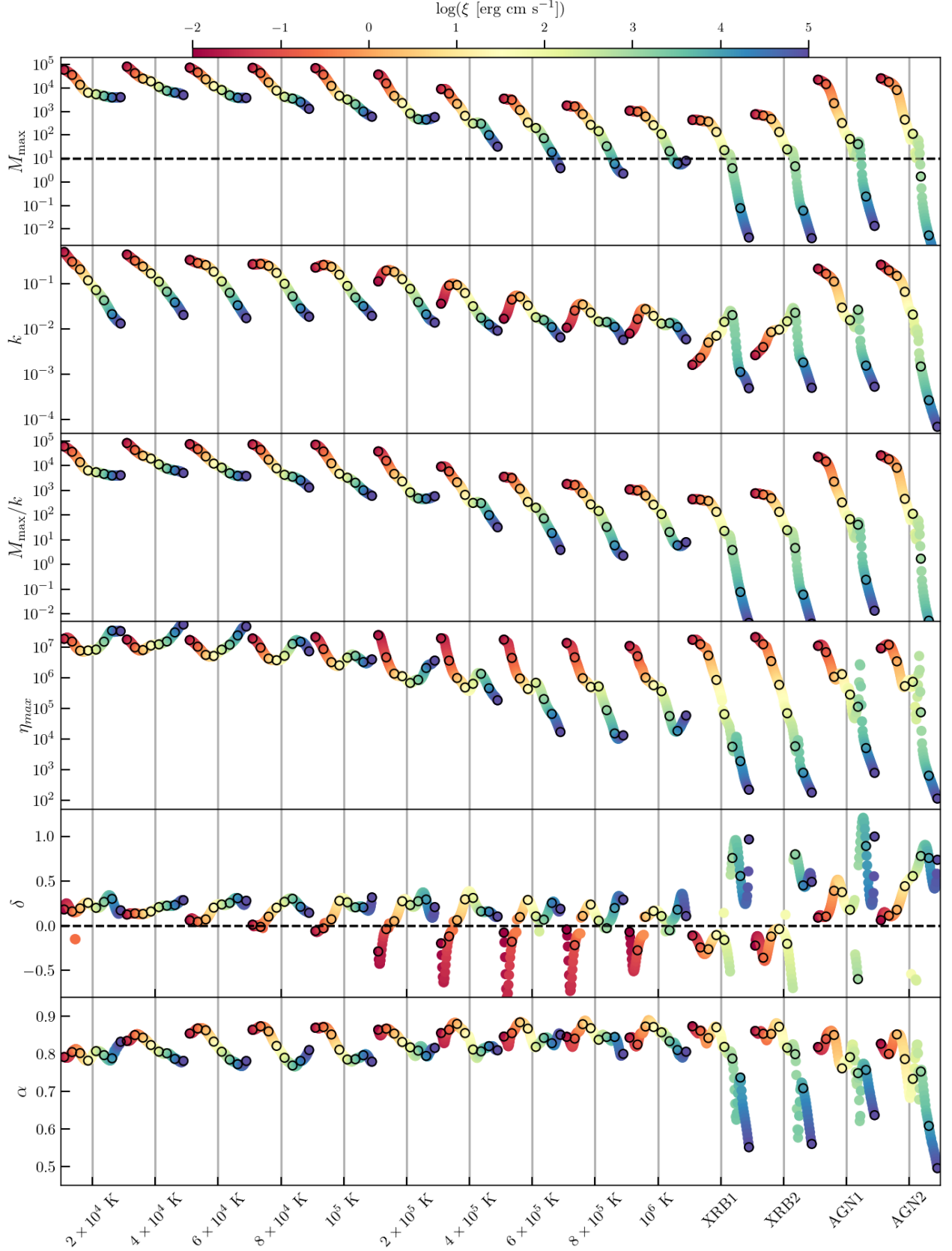


**Figure A.2.** Parameter survey of our line force results for the ten BB SEDs of different temperatures, XRB, and AGN SEDs with increasing mean photon energy from left to right. The parameters of interest from top to bottom are  $M_{max}$ ,  $k$ , the ratio of  $M_{max}$  and  $k$ , maximum line opacity  $\eta_{max}$ ,  $\alpha$ , and  $\delta$ . The color of each point corresponds to  $\log \xi$  shown in the color bar along the top (red corresponding to low ionization and blue with high ionization). The circled points correspond to where  $\log \xi = -2, -1, 0, 1, 2, 3, 4, 5$ , and the vertical lines are for reference but also indicate where  $\xi \approx 30$  for each SED.

that is,

$$\text{HEP}_0 = \frac{GM(1-\Gamma)}{r_0 c_s^2}, \quad (\text{B.6})$$

where  $M$  is the central mass,  $c_s$  the sound speed, and  $\Gamma$  is the luminosity in units of the Eddington luminosity  $L_{\text{Edd}}$ . For  $\text{HEP}_0 \lesssim 10$ , a thermally driven hydrodynamic (Parker) wind will be produced (e.g., [Stone & Proga 2009](#), and reference therein). This parameter is related to the density scale height of an isothermal static atmosphere,  $\lambda_\rho \equiv |\rho/(d\rho/dr)| = r_0/\text{HEP}_0$ . At the base of an outflowing atmosphere, the gas velocity is very sensitive to  $\text{HEP}_0$  for  $\text{HEP}_0 > \text{a few}$ , [i.e.,  $v_{0,\text{th}} \simeq c_s(\text{HEP}_0/2)^2 \exp(-\text{HEP}_0 + 3/2)$ , see e.g., [Lamers & Cassinelli \(1999\)](#)]. Thus the mass loss rate of the thermally driven wind also exponentially decreases with increasing  $\text{HEP}_0$  (i.e.,  $\dot{M}_{w,\text{th}} \simeq 4\pi r_0^2 \rho_0 v_0$ , where  $\rho_0$  is the gas density at the wind base.) This dimensionless parameter is also useful in measuring the strength of the thermal wind from an irradiated disk (see, e.g., [Waters et al. 2021](#)).

For line driving, such a measure of the wind strength should also exist but determining it is somewhat more involved. The basic requirement for line driving to dominate gravity is

$$M_{\text{max}}\Gamma \gtrsim 1, \quad (\text{B.7})$$

where  $M_{\text{max}}$  is the maximum value of the force multiplier for a given  $\xi$  when even most opaques lines are optically thin. The value of  $M_{\text{max}}$  could be as high as a few  $\times 10^3$  for low  $\xi$ , but it depends on  $\xi$  and can be viewed as the upper limit of  $M(t, \xi)$  when  $t$  approaches zero. However, the above requirement is just a necessary and not a sufficient condition for producing an appreciable line-driven wind, because the actual value of  $M$  can be smaller than  $M_{\text{max}}$  as the optical parameter is not always very much smaller than unity. Using the Sobolev approximation, [Castor et al. \(1975, CAK hereafter\)](#) showed that  $t \propto \rho/(dv_l/dl)$ . Thus more information is needed to compute the actual value of  $M$  than to compute  $M_{\text{max}}$ .

To estimate  $t$ , we will use the analytic expression for the mass-loss of the line-driven wind found by [CAK](#):

$$\dot{M}_{w,\text{CAK}} = \frac{4\pi GM(1-\Gamma)}{\sigma_e v_{\text{th}}} \left[ \frac{\alpha}{1-\alpha} \left( k_{\text{CAK}} \Gamma \frac{1-\alpha}{1-\Gamma} \right)^{1/\alpha} \right]. \quad (\text{B.8})$$

Next, we estimate the gas properties near the wind base where gas is gravitationally bound and subsonic so that the density radial profile is very close to the profile of an atmosphere in hydrostatic equilibrium ( $1/\lambda_\rho = -\text{HEP}_0/r_0$ ). On the other hand, using the mass continuity equation for a steady state, isothermal, spherical wind we have  $1/\lambda_\rho + 1/\lambda_v + 2/r = 0$  where  $\lambda_v = v/(dv/dr)$  is the velocity scale length which at the wind base can be approximated as  $\lambda_{v,0} \simeq r_0/(\text{HEP}_0 - 2)$ . Finally, using the last expression and the expressions for  $\dot{M}_{w,\text{CAK}}$  and  $t$ , we estimate the optical parameter at the wind base as

$$t_0 \simeq \tau_0^2 \frac{v_{\text{th}}^2}{c_s^2} \frac{1}{\text{HEP}_0(\text{HEP}_0 - 2)} \frac{1-\alpha}{\alpha} \left[ \frac{\Gamma}{1-\Gamma} k(1-\alpha) \right]^{-1/\alpha}, \quad (\text{B.9})$$

where  $\tau_0 = \sigma_e \rho_0 r_0$ . The  $\text{HEP}_0$  dependence in Eq. B.9 can be eliminated when we consider cases for  $\text{HEP}_0 > 2$  and use the definitions of  $\xi$  and  $\text{HEP}_0$ . Namely, using Eqs. 1 and B.6, we can write

$$\tau_0 = \frac{4\pi c k_B T_{\text{eq}}(\xi_0)}{\xi_0} \frac{\Gamma}{1-\Gamma} \text{HEP}_0 \quad (\text{B.10})$$

or introducing the so-called pressure ionization parameter,

$$\Xi = \xi/(4\pi c k_B T), \quad (\text{B.11})$$

we can rewrite it as

$$\tau_0 = \frac{\Gamma}{1-\Gamma} \frac{\text{HEP}_0}{\Xi_0}, \quad (\text{B.12})$$

to find that

$$t_0 \simeq \left( \frac{\Gamma}{1-\Gamma} \right)^2 \frac{1-\alpha}{\alpha} \left[ \frac{\Gamma}{1-\Gamma} k(1-\alpha) \right]^{-1/\alpha} \left( \frac{v_{\text{th}}}{c_s} \right)^2 \Xi_0^{-2}. \quad (\text{B.13})$$

Note that the sound speed is a function of  $\xi_0$  via the gas temperature (i.e., for thermal equilibrium  $\mathcal{L}(\xi_0, T_{\text{eq},0}) = 0$ ), whereas  $v_{th}$  is kept constant in calculations of  $k$  and  $\alpha$  (e.g., [Stevens & Kallman 1990](#)).

In [D20](#), we found that for given black hole mass  $M_{\text{BH}}$  and SED, three parameters govern the solutions:  $\Gamma$ ,  $\Xi_0$ , and  $\text{HEP}_0$ . These parameters set the strength of thermal driving, for example the mass loss of the thermal wind can be estimated as

$$\dot{M}_{w,th} = \frac{GM\Gamma}{4c_s\sigma_e} \frac{\text{HEP}_0^2}{\exp(\text{HEP}_0 - 3/2)} \Xi_0^{-1}. \quad (\text{B.14})$$

We could also estimate the optical depth parameter,  $t$ , at the base of a thermal wind,  $t_{0,th}$ . Using the same approach that we used to estimate  $t_0$  and expression for  $\dot{M}_{w,th}$ , we find

$$t_{0,th} = 4 \frac{1 - \Gamma}{\Gamma} \frac{\exp(\text{HEP}_0 - 3/2)}{\text{HEP}_0(\text{HEP}_0 - 2)} \frac{v_{th}}{c_s} \Xi_0^{-1}. \quad (\text{B.15})$$

Here, we show that two of these three dimensionless parameters, i.e.,  $\Gamma$  and  $\Xi_0$ , set also the strength of line driving, for given  $k$  and  $\alpha$ . Eq. [B.13](#) can be used to explain why line driving was negligible in the AGN cases we explored earlier. For the wind base to have a relatively low temperature so that the AGN-irradiated gas could be on a cold stable branch of the thermal equilibrium and to have many spectral lines,  $\Xi_0$  needs to be less than 10 (e.g., see Fig. 1 in [D20](#)). However, this does not lead to a large force multiplier because  $t$  at the base,  $t_0$  is not a free parameter: it decreases with increasing  $\Xi_0$  and therefore, it is large for small  $\Xi_0$ .

The line optical depth dependence on  $\Xi_0$  determines the parameter space for line driving in our self-consistent model: if  $\Xi_0$  is low enough for many lines to exist (i.e., large  $k$  and  $M_{\text{max}}$ ), the line optical depth could be too large for the line force to operate. To reduce the line's optical depth,  $\Xi_0$  would need to be increased but this could reduce the number of driving lines (i.e., small  $k$  and  $M_{\text{max}}$ ). Equation [B.15](#) shows that  $t$  at the base at a thermally driven wind exponentially increases with  $\text{HEP}_0$  for large  $\text{HEP}_0$  which implies that as the thermal wind weakens with increasing  $\text{HEP}_0$ , the line driving may not necessarily kick in and strengthen the wind because the gas could be too optically thick unless  $\Xi$  or  $c_s$  or both increase.

In the two AGN cases explored in [D20](#), we found that there is no parameter space for which  $M(t, \xi) \Gamma > \text{exceeds } 1$ . This is despite the fact that for a wide range of  $\xi$  values, the necessary condition for line driving is satisfied. In section [§3](#), we present specific examples of BB SED cases that meet not only the necessary condition stated in inequality [B.7](#) but also the  $M(t, \xi) \Gamma > 1$  condition. These cases can have a BB temperature,  $T_{\text{BB}}$ , as high as  $10^6$  K.

## REFERENCES

- Abbott, D. C. 1982, *ApJ*, 259, 282, doi: [10.1086/160166](#)
- Arav, N., & Li, Z.-Y. 1994, *ApJ*, 427, 700, doi: [10.1086/174177](#)
- Blandford, R. D., & Payne, D. G. 1982, *MNRAS*, 199, 883, doi: [10.1093/mnras/199.4.883](#)
- Bowler, R. A. A., Hewett, P. C., Allen, J. T., & Ferland, G. J. 2014, *MNRAS*, 445, 359, doi: [10.1093/mnras/stu1730](#)
- Castor, J. I. 2007, *Radiation Hydrodynamics*
- Castor, J. I., Abbott, D. C., & Klein, R. I. 1975, *ApJ*, 195, 157, doi: [10.1086/153315](#)
- Clarke, C., & Carswell, B. 2014, *Principles of Astrophysical Fluid Dynamics*
- Curé, M., Cidale, L., & Granada, A. 2011, *ApJ*, 737, 18, doi: [10.1088/0004-637X/737/1/18](#)
- Dannan, R. C., Proga, D., Kallman, T. R., & Waters, T. 2019, *ApJ*, 882, 99, doi: [10.3847/1538-4357/ab340b](#)
- Dannan, R. C., Proga, D., Waters, T., & Dyda, S. 2020, *ApJL*, 893, L34, doi: [10.3847/2041-8213/ab87a5](#)
- de Kool, M., & Begelman, M. C. 1995, *ApJ*, 455, 448, doi: [10.1086/176594](#)
- Dyda, S., Dannen, R., Waters, T., & Proga, D. 2017, *MNRAS*, 467, 4161, doi: [10.1093/mnras/stx406](#)
- Dyda, S., Proga, D., & Reynolds, C. S. 2020, *MNRAS*, 493, 437, doi: [10.1093/mnras/staa304](#)
- Field, G. B. 1965, *ApJ*, 142, 531, doi: [10.1086/148317](#)
- Foltz, C. B., Weymann, R. J., Morris, S. L., & Turnshek, D. A. 1987, *ApJ*, 317, 450, doi: [10.1086/165290](#)
- Frank, J., King, A., & Raine, D. J. 2002, *Accretion Power in Astrophysics: Third Edition*
- Ganguly, R., Masiero, J., Charlton, J. C., & Sembach, K. R. 2003, *ApJ*, 598, 922, doi: [10.1086/379057](#)
- Giustini, M., & Proga, D. 2019, *A&A*, 630, A94, doi: [10.1051/0004-6361/201833810](#)
- Gupta, N., Srianand, R., Petitjean, P., & Ledoux, C. 2003, *A&A*, 406, 65, doi: [10.1051/0004-6361:20030793](#)
- Higginbottom, N., Proga, D., Knigge, C., et al. 2014, *ApJ*, 789, 19, doi: [10.1088/0004-637X/789/1/19](#)

- Jiang, Y.-F. 2022, *ApJS*, 263, 4,  
doi: [10.3847/1538-4365/ac9231](https://doi.org/10.3847/1538-4365/ac9231)
- Kallman, T., & Bautista, M. 2001, *ApJS*, 133, 221,  
doi: [10.1086/319184](https://doi.org/10.1086/319184)
- Krolik, J. H. 1999, *Active galactic nuclei : from the central black hole to the galactic environment*
- Kurosawa, R., & Proga, D. 2009, *ApJ*, 693, 1929,  
doi: [10.1088/0004-637X/693/2/1929](https://doi.org/10.1088/0004-637X/693/2/1929)
- Lamers, H. J. G. L. M., & Cassinelli, J. P. 1999, *Introduction to Stellar Winds*
- Lu, W.-J., & Lin, Y.-R. 2018, *ApJ*, 863, 186,  
doi: [10.3847/1538-4357/aad411](https://doi.org/10.3847/1538-4357/aad411)
- Mas-Ribas, L., & Mauland, R. 2019, *ApJ*, 886, 151,  
doi: [10.3847/1538-4357/ab4efd](https://doi.org/10.3847/1538-4357/ab4efd)
- Mehdipour, M., Kaastra, J. S., Kriss, G. A., et al. 2015, *A&A*, 575, A22, doi: [10.1051/0004-6361/201425373](https://doi.org/10.1051/0004-6361/201425373)
- Mihalas, D., & Mihalas, B. W. 1984, *Foundations of radiation hydrodynamics*
- Murray, N., Chiang, J., Grossman, S. A., & Voit, G. M. 1995, *ApJ*, 451, 498, doi: [10.1086/176238](https://doi.org/10.1086/176238)
- Mushotzky, R. F., Solomon, P. M., & Strittmatter, P. A. 1972, *ApJ*, 174, 7, doi: [10.1086/151463](https://doi.org/10.1086/151463)
- Nomura, M., Ohsuga, K., & Done, C. 2020, *MNRAS*, 494, 3616, doi: [10.1093/mnras/staa948](https://doi.org/10.1093/mnras/staa948)
- Nomura, M., Ohsuga, K., Wada, K., Susa, H., & Misawa, T. 2013, *PASJ*, 65, 40, doi: [10.1093/pasj/65.2.40](https://doi.org/10.1093/pasj/65.2.40)
- North, M., Knigge, C., & Goad, M. 2006, *MNRAS*, 365, 1057, doi: [10.1111/j.1365-2966.2005.09828.x](https://doi.org/10.1111/j.1365-2966.2005.09828.x)
- Owocki, S. P., Castor, J. I., & Rybicki, G. B. 1988, *ApJ*, 335, 914, doi: [10.1086/166977](https://doi.org/10.1086/166977)
- Owocki, S. P., Cranmer, S. R., & Blondin, J. M. 1994, *ApJ*, 424, 887, doi: [10.1086/173938](https://doi.org/10.1086/173938)
- Proga, D. 1999, *MNRAS*, 304, 938,  
doi: [10.1046/j.1365-8711.1999.02408.x](https://doi.org/10.1046/j.1365-8711.1999.02408.x)
- . 2007, *ApJ*, 661, 693, doi: [10.1086/515389](https://doi.org/10.1086/515389)
- Proga, D., & Kallman, T. R. 2004, *ApJ*, 616, 688,  
doi: [10.1086/425117](https://doi.org/10.1086/425117)
- Proga, D., Stone, J. M., & Drew, J. E. 1998, *MNRAS*, 295, 595, doi: [10.1046/j.1365-8711.1998.01337.x](https://doi.org/10.1046/j.1365-8711.1998.01337.x)
- . 1999, *MNRAS*, 310, 476,  
doi: [10.1046/j.1365-8711.1999.02935.x](https://doi.org/10.1046/j.1365-8711.1999.02935.x)
- Proga, D., Stone, J. M., & Kallman, T. R. 2000, *ApJ*, 543, 686, doi: [10.1086/317154](https://doi.org/10.1086/317154)
- Puls, J., Springmann, U., & Lennon, M. 2000, *A&AS*, 141, 23, doi: [10.1051/aas:2000312](https://doi.org/10.1051/aas:2000312)
- Quera-Bofarull, A., Done, C., Lacey, C. G., Nomura, M., & Ohsuga, K. 2021, *arXiv e-prints*, arXiv:2111.02742.  
<https://arxiv.org/abs/2111.02742>
- Shu, F. H. 1992, *The physics of astrophysics. Volume II: Gas dynamics*.
- Sim, S. A., Proga, D., Miller, L., Long, K. S., & Turner, T. J. 2010, *MNRAS*, 408, 1396,  
doi: [10.1111/j.1365-2966.2010.17215.x](https://doi.org/10.1111/j.1365-2966.2010.17215.x)
- Srianand, R., Petitjean, P., Ledoux, C., & Hazard, C. 2002, *MNRAS*, 336, 753, doi: [10.1046/j.1365-8711.2002.05792.x](https://doi.org/10.1046/j.1365-8711.2002.05792.x)
- Stevens, I. R., & Kallman, T. R. 1990, *ApJ*, 365, 321,  
doi: [10.1086/169486](https://doi.org/10.1086/169486)
- Stone, J. M., & Proga, D. 2009, *ApJ*, 694, 205,  
doi: [10.1088/0004-637X/694/1/205](https://doi.org/10.1088/0004-637X/694/1/205)
- Stone, J. M., Tomida, K., White, C. J., & Felker, K. G. 2020, *ApJS*, 249, 4, doi: [10.3847/1538-4365/ab929b](https://doi.org/10.3847/1538-4365/ab929b)
- Trigo, M. D., Boirin, L., Migliari, S., et al. 2013, in *Feeding Compact Objects: Accretion on All Scales*, ed. C. M. Zhang, T. Belloni, M. Méndez, & S. N. Zhang, Vol. 290, 25–28
- Wang, B.-C., Yang, X.-H., Bu, D.-F., & Huang, S.-S. 2022, *MNRAS*, 515, 5594, doi: [10.1093/mnras/stac2203](https://doi.org/10.1093/mnras/stac2203)
- Waters, T., & Proga, D. 2016, *MNRAS*, 460, L79,  
doi: [10.1093/mnrasl/slw056](https://doi.org/10.1093/mnrasl/slw056)
- Waters, T., Proga, D., & Dannen, R. 2021, *ApJ*, 914, 62,  
doi: [10.3847/1538-4357/abfbef6](https://doi.org/10.3847/1538-4357/abfbef6)